



Chinese Society of Aeronautics and Astronautics
& Beihang University

Chinese Journal of Aeronautics

cja@buaa.edu.cn
www.sciencedirect.com



Effects of fiber orientation on tool wear evolution and wear mechanism when cutting carbon fiber reinforced plastics

Weizhou WU^a, Shipeng LI^{a,*}, Xuda QIN^a, Wentao LIU^a, Xin CUI^b, Hao LI^a, Mengrui SHI^a, Haibao LIU^c

^a Key Laboratory of Mechanism Theory and Equipment Design of Ministry of Education, Tianjin University, Tianjin 300350, China

^b Tianjin Aerospace Long March Launch Vehicle Manufacturing Co. Ltd, Tianjin 30000, China

^c Centre for Aeronautics, School of Aerospace, Transport and Manufacturing, Cranfield University, Cranfield MK43 0AL, UK

Received 29 April 2022; revised 6 July 2022; accepted 29 July 2022

KEYWORDS

Carbon fiber reinforced plastics (CFRP);
Fiber orientation;
Finite element method (FEM);
Tool wear;
Wear mechanism

Abstract The aim of the present paper is to reveal the influence of different fiber orientations on the tool wear evolution and wear mechanism. Side-milling experiments with large-diameter milling tools are conducted. A finite element (FE) cutting model of carbon fiber reinforced plastics (CFRP) is established to get insight into the cutting stress status at different wear stages. The results show that different fiber orientations bring about distinct differences in the extent, profile and mechanism of tool wear. Severer wear occurs when cutting 45° and 90° plies, followed by 0°, correspondingly, the least wear is obtained when $\theta = 135^\circ$ (θ represents the orientation of fibers). Moreover, the worn profiles of cutting tools when $\theta = 0^\circ$ and 45° are waterfall edge, while round edge occurs when $\theta = 135^\circ$ and a combined shape of waterfall and round edge is obtained when $\theta = 90^\circ$. The wear mechanisms under different fiber orientations are strongly dependent on the cutting stress distributions. The evolution of tool wear profile is basically consistent with the stress distribution on the tool surface at different wear stages, and the extent of tool wear is determined by the magnitude of stress on the tool surface. Besides, the worn edges produce an actual negative clearance angle, which decreases the actual cutting thickness and leads to compressing and bending failure of fibers beneath the cutting region as well as low surface qualities.

© 2022 Chinese Society of Aeronautics and Astronautics. Production and hosting by Elsevier Ltd. This is an open access article under the CC BY-NC-ND license (<http://creativecommons.org/licenses/by-nc-nd/4.0/>).

* Corresponding author.

E-mail address: shipengli@tju.edu.cn (S. LI).

Peer review under responsibility of Editorial Committee of CJA.



1. Introduction

Due to the high strength-to-weight ratios, modulus-to-weight ratios, good wear resistance and good corrosion resistance, carbon fiber reinforced plastic (CFRP) is greatly utilized in aerospace industry, transportation and health care¹⁻⁴. CFRP parts usually need lots of machining to meet the size and shape

<https://doi.org/10.1016/j.cja.2022.09.003>

1000-9361 © 2022 Chinese Society of Aeronautics and Astronautics. Production and hosting by Elsevier Ltd.

This is an open access article under the CC BY-NC-ND license (<http://creativecommons.org/licenses/by-nc-nd/4.0/>).

Please cite this article in press as: WU W et al. Effects of fiber orientation on tool wear evolution and wear mechanism when cutting carbon fiber reinforced plastics, *Chin J Aeronaut* (2023), <https://doi.org/10.1016/j.cja.2022.09.003>

requirements.⁵ But CFRP is a kind of typical hard-to-machining material, machining damage easily occurs and is very sensitive to tool wear. While the hard carbon fibers dramatically accelerate the tool wear. Thus, tool wear is one of the most important factors for high quality machining of CFRP.^{6,7}

It is well known that the fiber orientation has a significant impact on CFRP cutting process. Cutting mechanism under different fiber orientations has been studied by many scholars in the past decades. Wang et al.⁸ investigated the mechanisms of orthogonal cutting of unidirectional Gr/Ep and found that material removal was primarily dependent on the fiber orientation, three different cutting mechanisms were discussed in 0° fiber orientation, positive fiber orientation up to 70° and negative fiber orientations. An et al.⁹ investigated the chip formation process and its effect on the machined surface, different cutting mechanisms at various fiber orientations were discussed. A three-dimension micro-scale cutting simulation model was established by Meng et al.,¹⁰ variation of cutting mechanism was analyzed and summarized into tearing type, crushing type and bending type.

In addition to the cutting mechanism, the tool wear mechanism in machining of carbon fiber reinforced plastics has been investigated. Rawat and Attia¹¹ studied the wear mechanism of tungsten carbide in drilling woven graphite fiber epoxy composites at high speed and analyzed the effect of tool wear on cutting force and tool quality. Fracture at the beginning of drilling process, following abrasion and possibly adhesion were found to be the main wear mechanisms. Azmi et al.¹² studied the wear mechanism of uncoated tungsten carbide tools using end milling tests of GFRP composites, they observed that the failure mechanism was due to abrasion on the flank face. Ramirez et al.¹³ highlighted the effects of tool wear on cutting forces and temperatures, and also found that abrasion was the main wear mechanism during drilling CFRP.

In view of the influence of fiber orientation on cutting mechanism, tool wear will also vary with different orientations. Some scholars investigated the relationship between fiber orientation and tool wear in cutting of CFRP. Maegawa et al.¹⁴ conducted down-milling experiments of unidirectional and cross-directional CFRP and found that fiber orientation in the CFRP laminates relative to the tool-traveling direction is an important factor to the tool wear process. The tool-edge height was defined to explain the relationship between worn edge profiles and the surface roughness. Nguyen et al.¹⁵ studied the impact of fiber orientation on tool wear by conducting edge-trimming experiments with particular ply angles of 0°, 45°, 90° and 135° under different spindle speeds. They found that cutting speed affects all wear characteristics regardless of the ply angle, and the 45° plies resulted in extensive flank wear while the 0° plies had the least amount of tool wear. In summary, most of the studies on the relationship between fiber orientation and tool wear in cutting of CFRP only give the experimental results, less of them conduct detailed analysis of wear evolution and mechanisms. In this paper, side-milling experiments with large-diameter milling tools are conducted. A microscopic cutting model of CFRP was established. The effects of fiber orientation on tool wear evolution, wear mechanism and cutting quality were studied. The cutting stress at different wear stages in cutting of CFRP with different fiber angles were particularly extracted and discussed compared

with the worn profiles of cutting tool. The changes in cutting mechanisms of fibers caused by tool wear were also analyzed.

2. Modeling

A 2D micro cutting model was established to simulate the orthogonal cutting process, which was capable to reveal the stress distribution and material removal in the cutting process well.^{16–19} Considering the structure of CFRP, the model was mainly composed of three phases: carbon fiber, epoxy matrix and interface phase.²⁰ In order to conform to the actual processing situation, the width of fiber in the model is 7 μm, corresponding actual fiber diameter is 7 μm. In the area away from the cutting zone, equivalent homogeneous material (EHM) was used to reduce the calculation cost and provide a supporting function, as shown in Fig. 1.

Carbon fiber was considered as a transversely anisotropic material, the failure initiation was characterized by the 2D Hashin criterion as formulated in Eq. (1).²¹ Because of its brittle property, there was almost no degradation stage.

$$\text{Longitudinal tensile}(\sigma_1 \geq 0): \left(\frac{\sigma_1}{X_t}\right)^2 + \left(\frac{\tau_{12}}{S_{12}}\right)^2 \geq 1$$

$$\text{Longitudinal compressive}(\sigma_1 < 0): \left(\frac{\sigma_1}{X_c}\right)^2 \geq 1$$

$$\text{Transverse tensile}(\sigma_2 \geq 0): \left(\frac{\sigma_2}{Y_t}\right)^2 + \left(\frac{\tau_{12}}{S_{12}}\right)^2 \geq 1$$

$$\text{Transverse compressive}(\sigma_2 < 0): \left(\frac{\sigma_2}{Y_c}\right)^2 + \left(\frac{\tau_{12}}{S_{12}}\right)^2 \geq 1 \quad (1)$$

where, X_t , X_c , Y_t and Y_c denote the longitudinal tensile strength, longitudinal compressive strength, transverse tensile strength and transverse compressive strength, respectively. S_{12} denote the shear strength of carbon fiber.

Different from the fiber, the epoxy matrix exhibits elastic-plastic behavior. The stress-strain relationship in elastic stage is considered to be linear and satisfies generalized Hooke's law. The Johnson-Cook constitutive model was used to describe its plastic stage, as reported in Eq. (2). The DUCTILE failure criterion was utilized to characterize the failure of matrix.

$$\bar{\sigma} = \left[A + B \bar{\epsilon}_p^{-n} \right] [1 + C \ln \dot{\epsilon}^*] [1 - T^{*m}] \quad (2)$$

where, $\bar{\sigma}$ is the equivalent stress, $\bar{\epsilon}_p^{-n}$ is the equivalent plastic strain, $\dot{\epsilon}^* = \dot{\epsilon}/\dot{\epsilon}_0$, $\dot{\epsilon}_0$ is the reference strain rate. $T^* = (T - T_r)/(T_m - T_r)$, where, T_r is the room temperature, T_m is the melting point of the material. A , B , C , n and m are the parameters determined through experiments.

The interfacial phase between fiber and matrix was realized by zero-thickness cohesive element in Abaqus using traction-separation law, which was considered to be failed when the absorbed energy reached the fracture energy. All of the parameters were obtained from the previous literatures (see Table 1).

In the FE model, the deformable body was established in the front of the tool in this paper to get the stress distribution on the tool, and the movement was realized by the rigid body behind it, as shown in Fig. 1. It is worth noting that in order to obtain accurate stress distribution, the tool profiles in the simulation were obtained from the experiments, and then imported to Abaqus. The friction coefficient between tool and workpiece was set to 0.3.¹⁷ COH2D4 element was used for interface phase, and CPS4R was used for other parts. In

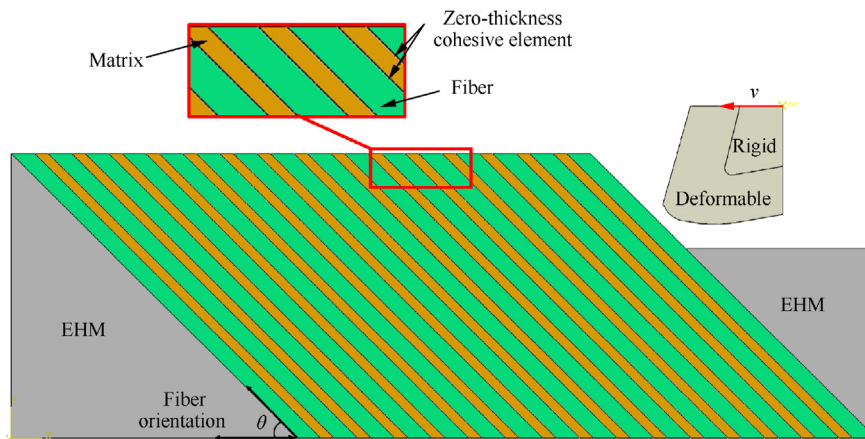


Fig. 1 Schematic of 2D FEM model when $\theta = 45^\circ$.

Table 1 Material properties of CFRP in simulation.^{22–24}

Material	Property	Value
Carbon fiber	Elastic constants	$E_1 = 235 \text{ GPa}, E_2 = 14 \text{ GPa}, \mu_{12} = 0.25, G_{12} = 2.8 \text{ GPa}$
	Longitudinal strength	$X_T = 4.62 \text{ GPa}, X_C = 3.96 \text{ GPa}$
	Transverse strength	$Y_T = 1.5 \text{ GPa}, Y_C = 3.34 \text{ GPa}$
	Shear strength	$S_{12} = 1.5 \text{ GPa}$
	Density	$\rho_f = 1.47 \text{ g/cm}^3$
Epoxy	Elastic constants	$E = 3.4 \text{ GPa}, \mu = 0.35$
	Fracture energy	0.15 mJ/mm^2
	Johnson-Cook params	$A = 120 \text{ MPa}, B = 654.18 \text{ MPa}, C = 0.124, m = 0.304, n = 0.772$
	Density	$\rho_c = 1.2 \text{ g/cm}^3$
Interface	Normal stress	$t_N = 50 \text{ MPa}$
	Shear stress	$t_S = 75 \text{ MPa}$
	Elastic stiffness	$K = 10^8 \text{ N/mm}^3$
	Fracture energy	$G_N = 0.015 \text{ mJ/mm}^2, G_S = 0.045 \text{ mJ/mm}^2$
EHM	Elastic constants	$E = 135 \text{ GPa}, \mu = 0.318$
Tool	Elastic constants	$E = 630 \text{ GPa}, \mu = 0.3$

order to ensure the accuracy of the results, the mesh scale in cutting zone was $1 \mu\text{m} \times 1 \mu\text{m}$.

In order to quantitatively compare the tool surface stress under different fiber orientations and wear stages, paths were defined along the tool surfaces, and then the stress on the paths were extracted, as shown in Fig. 2.

3. Set up of the experiment

3.1. Workpiece material

Unidirectional CFRP (UD-CFRP) plates with T700 carbon fibers ($\sim 60\%$ volume fraction) and epoxy resin were used as the workpiece. The size of the plates were $170 \text{ mm} \times 120 \text{ mm} \times 5 \text{ mm}$. In the case of $\theta = 135^\circ$, seriously splitting occurred in the cutting process, as shown in Fig. 3(a). So two 0° plies of 2.5 mm were placed on both sides of the 135° ply of 5 mm , as shown in Fig. 3(b). The cutting forces of 135° plate were calculated by the measured forces when cutting the

combinatorial plate subtracting the forces when cutting the two single 0° plates.

3.2. Experimental setup and cutting conditions

The traditional orthogonal cutting experiment is not consistent with the actual cutting process because of the low cutting speed. In this paper, considering the high cutting speed and the unicity of fiber orientation, large-diameter side-milling experiments were conducted. The diameter of the milling tool was much larger than the width of milling, so it was very close to high-speed orthogonal cutting. A 5-axis DMG machining center was used to carry out the experiments and a Kistler dynamometer was used to record the cutting forces, as shown in Fig. 4.

Uncoated tungsten carbides inserts were used in the experiments. In order to eliminate the installation error of inserts, only one insert was installed on the holder at the same time. There was no any cooling device in the cutting process. Cutting

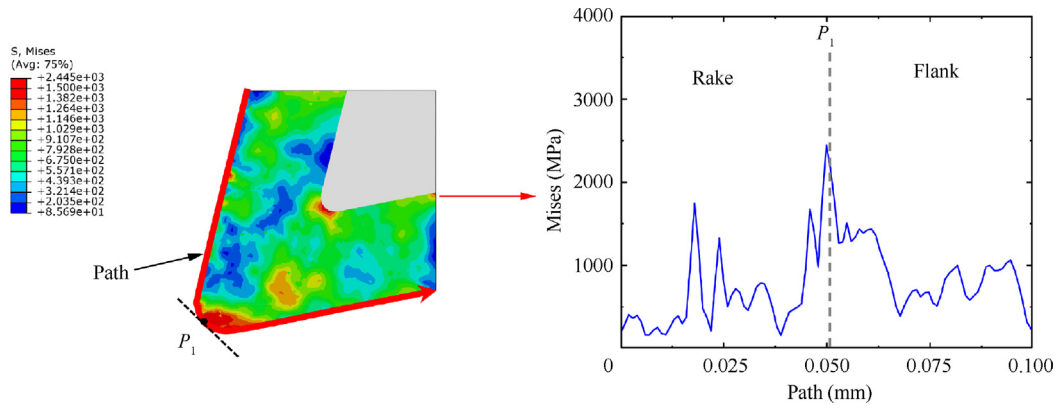


Fig. 2 Schematic diagram of surface stress.

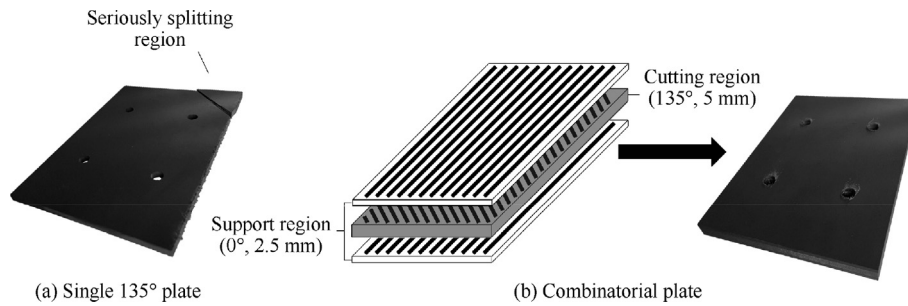


Fig. 3 Schematic diagram of plate.

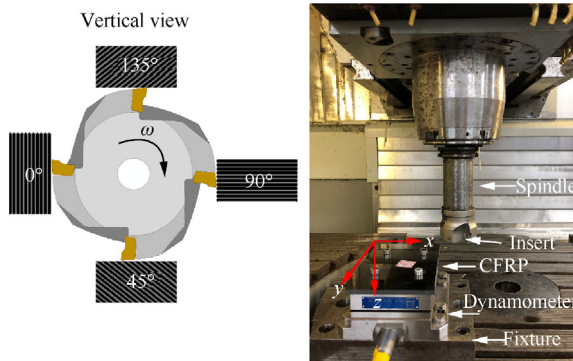


Fig. 4 Set up of experiment equipment.

parameters were set to be constant, as listed in Table 2. In order to analyze the tool evolution, the tools after feeding 25, 50, 75, 100, 125, 150, 200, 300, 500, 1000 mm were observed and measured.

3.3. Measurement

Cutting forces during the machining process were measured by dynamometer (Kistler), it could record the force and moment of three vertical directions at the same time. A series of 2D tool profiles were obtained by an edge-profile measurement instrument (IF-Edgemaster produced by Alicona) as shown in Fig. 5, from which the evolution of tool wear could be ana-

lyzed. Scanning electron microscopy (SEM) was used to observe the tiny details on the cutting edge and the machined surface. To avoid the influence of residual chips, all tools were cleaned by ultra-sonication in alcohol for 30 minutes before measurement.

Different features of worn edge profiles were recognized based on the 2D tool profiles. According to Raj and Karunamoorthy article,²⁵ peak flattening (PF), flank rounding depth (FRD), flank rounding width (FRW), flank wear (VB) and cutting edge radius (CER) were used to characterize tool wear in this study. The schematic diagram is shown in Fig. 6. Where, P_0 is the intersection point of two least squares fitting lines of rake face and flank face, P_1 is the peak point of tool profile, a horizontal line is generated through P_1 , then the line is translated downward by $0.5 \mu\text{m}$ and intersects with the profile at two points, P_2 and P_3 ($0.5 \mu\text{m}$ is reported to be the highest repeatability value). The characters were defined by these points.

4. Result and discussion

4.1. Analysis of cutting force

Fig. 7 shows the schematic of up-milling process, the forces in X and Y direction were obtained directly by the dynamometer. Then, cutting forces were decomposed into cutting force F_C and thrust force F_T , along the direction tangent to and perpendicular to the tool movement, respectively. It can be obtained by Eq. (3):

Table 2 Experimental cutting condition.

Tool	Value	Machining conditions	Value
Material	WC/Co	Spindle speed n_s (r/min)	600
Clearance angle α (°)	11	Cutting speed v (m/min)	120
Rake angle γ (°)	14	Feed rate f (mm/tooth)	0.03
Cutting edge radius r_c (μm)	~ 7	Number of tooth	1
Coating	None	Depth of milling a_p (mm)	5
Tool diameter d (mm)	63	Width of milling a_c (mm)	2
		Coolant	None

$$\begin{cases} F_C = \int_0^{\varphi_{\max}} (F_y \cos \varphi - F_x \sin \varphi) d\varphi / \varphi_{\max} \\ F_T = \int_0^{\varphi_{\max}} (F_y \sin \varphi + F_x \cos \varphi) d\varphi / \varphi_{\max} \end{cases} \quad (3)$$

where φ is the angle between the tool and the vertical feed direction in the cutting process. From the milling tool diameter is 63 mm and the milling width is 2 mm, the value of $\varphi_{\max} = 20.56^\circ$ can be calculated.

Fig. 8 shows the cutting forces under different fiber orientations. Generally, the thrust force is much larger than the cutting force, which is consistent to the results in previous literature.^{26–28} Cutting force increase with the feeding. At the beginning of process, there are apparent differences in cutting forces at different orientations. The cutting force produced by 90° ply is the largest, followed by 45° , while the cutting forces produced by 0° and 135° are significantly less than that of the previous two angles. This is considered to be related to the cutting mechanism at various fiber orientations. When $\theta = 0^\circ$, the main fracture mode of fiber is excessive bending,²⁹ fibers ahead of the cutting tool fail once the bending stresses exceed the failure stress.³⁰ For the 45° and 90° plies, the fibers undergo a crush-dominated failure at the contact point of the tool, the bending stresses in the fibers can also be observed below the cutting plane.³⁰ When fiber orientation is 135° , the fibers are bent to failure by the movement of rake surface, because the failure point is below the cutting surface, the “burst” type chips are formed.⁹ Since the failure mode of fiber is dictate the cutting force, the crushing-dominated failure requires more cutting force than the bending failure,³⁰ so the cutting forces at 45° and 90° are relatively large. It can also be verified by the

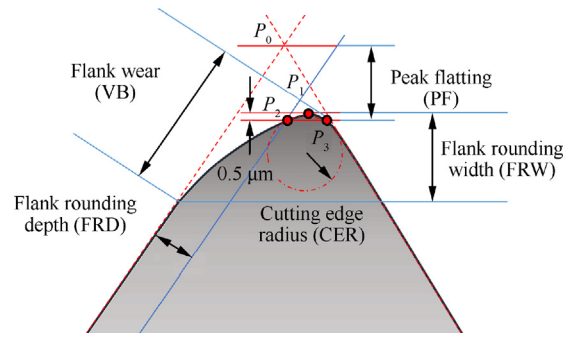


Fig. 6 Features of worn tools.

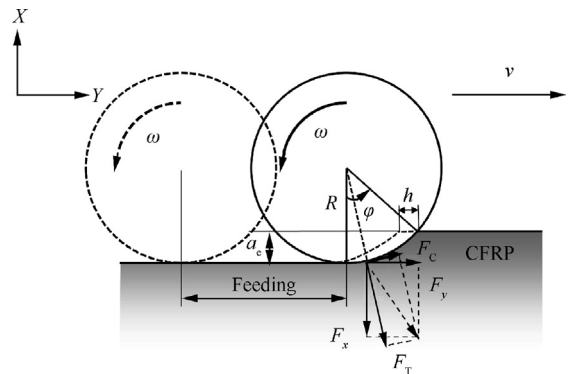


Fig. 7 Schematic of up-milling configuration.

numerical simulations, the cutting forces are 13.65, 31.48, 32.73, 20.02 N in order (the value is the average value of the cutting force in the stable stage). However, as the tool wear, the cutting forces at 90° and 45° reach the same level, this is due to the similar cutting mechanism after tool wear, more fibers are bent to failure when the tool wear severely as discussed in the following sections. For the thrust force, there are some differences. At the beginning, the thrust force at 45° ply is the largest, then 90° , 0° and 135° , this is reported to be related to the spring back of carbon fibers.²⁸ With the wear of tool, the thrust force at 0° becomes larger than that at 90° . The increased negative flank angle of tool after wear causes a larger thrust force from the fibers. In sum, the differences in cutting and thrust forces are mainly related to the dif-

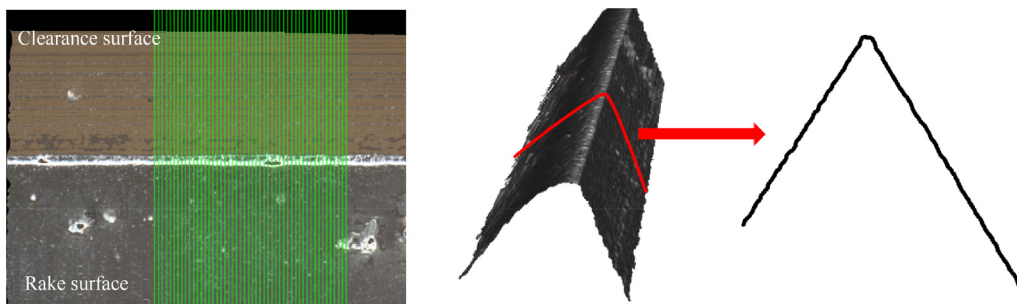


Fig. 5 Profile obtained from edgmaster.

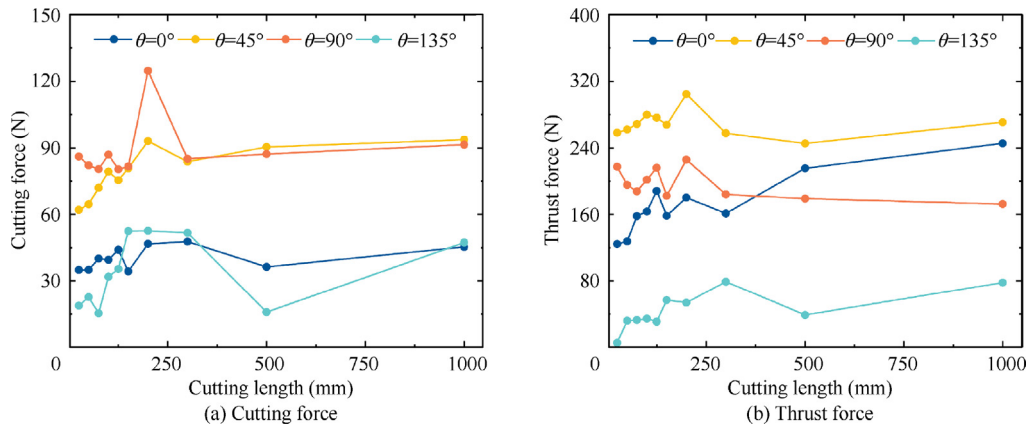


Fig. 8 Cutting force and thrust force under 0° , 45° , 90° and 135° orientation.

ferent cutting mechanisms of CFRP in different tool wear stages.

4.2. Evolution of the edge profiles with tool wear

The 2D profiles of the fresh tool and worn tools after feeding 25, 50, 75, 100, 125, 150, 200, 300, 500 and 1000 mm under different fiber orientations are shown in Fig. 9. It can be seen that the tool profiles when cutting different orientations are significantly dif-

ferent. The obvious waterfall edges are obtained when $\theta = 0^\circ$ and 45° , while the round edges formed when $\theta = 135^\circ$. The worn edge profiles at 90° are the combined shape of waterfall and round edges. In order to quantitatively analyze the tool wear, the method as depicted in Fig. 6 was used to extract tool features, and the results are shown in Fig. 9, the wear area was also introduced to measure the extent of wear.

In terms of wear area as shown in Fig. 10(f), cutting 90° ply produced the most severe wear, then 45° and 0° , while 135° ply

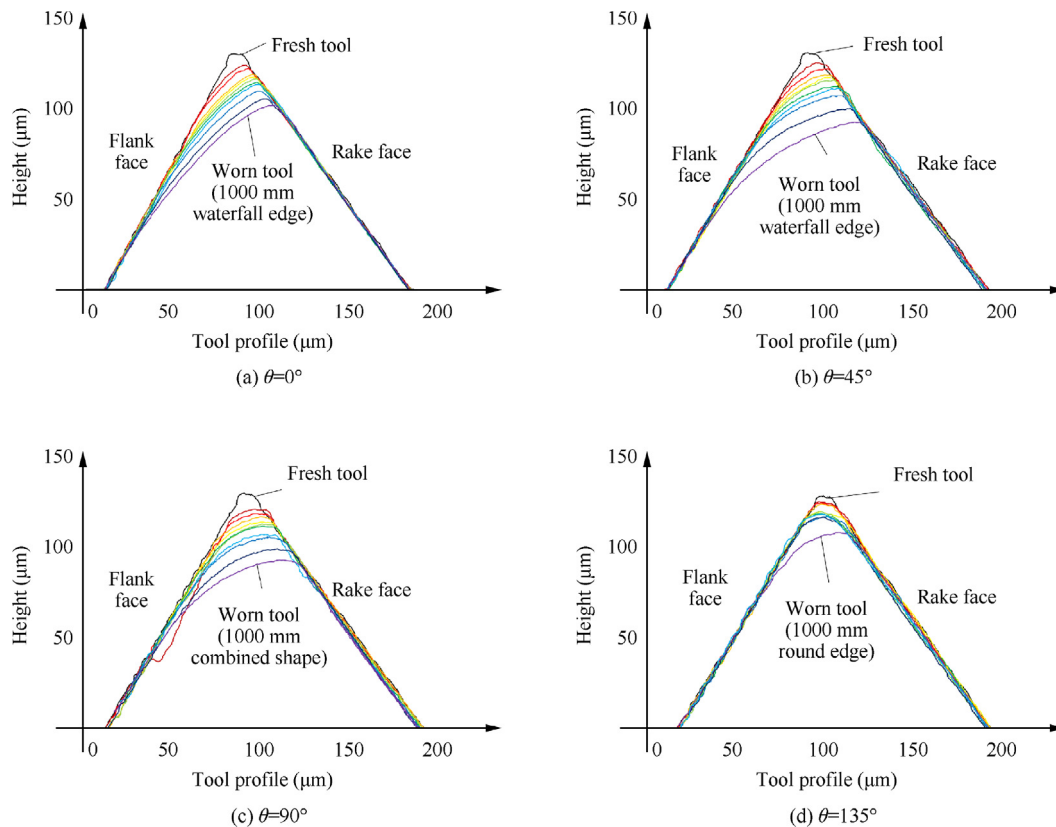


Fig. 9 Tool wear profiles under four different fiber orientations.

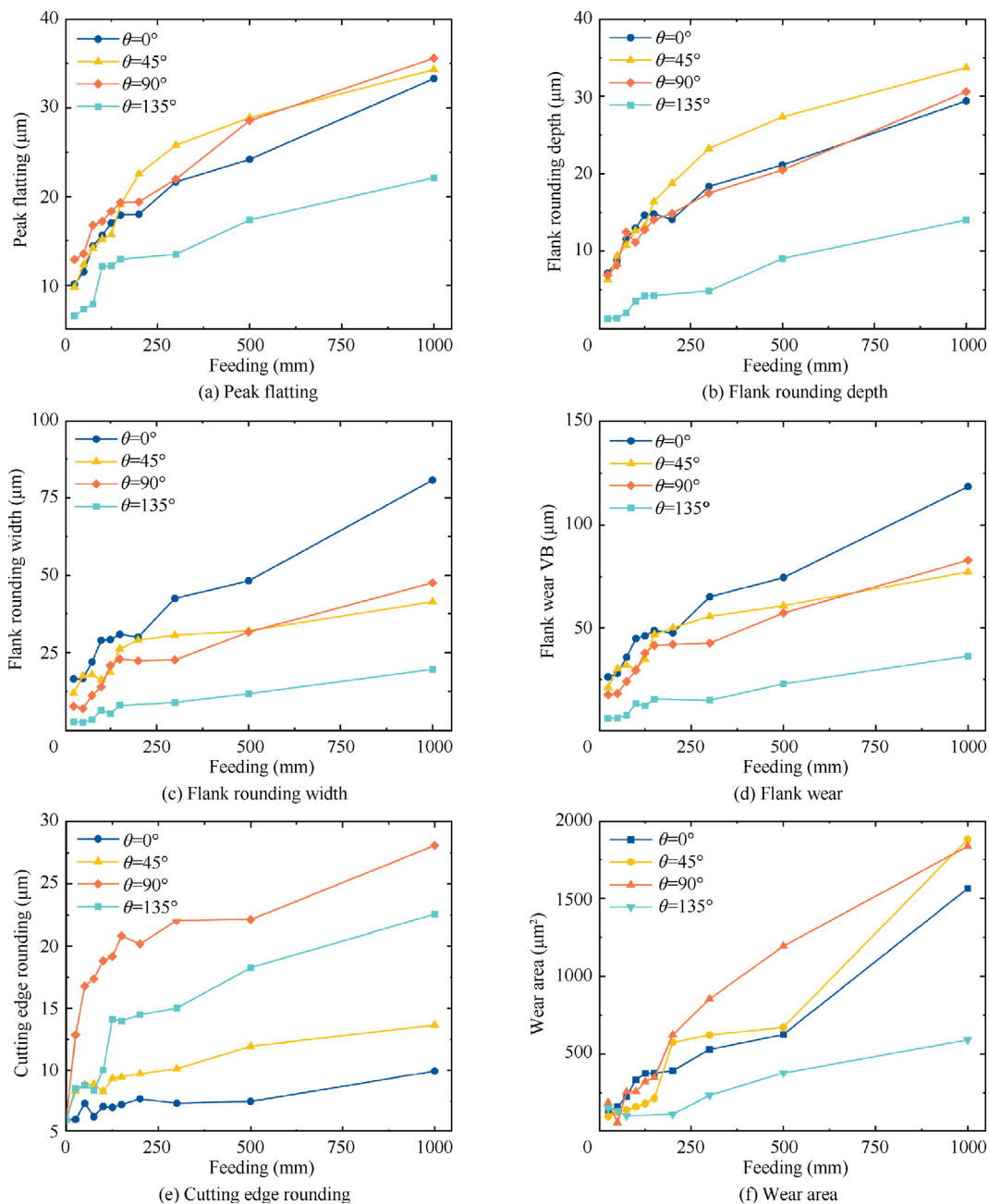


Fig. 10 Quantitative indexes of tool wear.

produced the least tool wear. Generally, the flank wear is much severer than the rake wear regardless of fiber orientation, although the worn profiles are obviously distinct. When $\theta = 0^\circ$, VB and FRW are larger than other orientations (see Fig. 10(c) and (d)), which means that the length of contact area between flank face and workpiece is the largest. Meanwhile, the CER is the least because of the waterfall profile. As for $\theta = 45^\circ$, the FRD and PF are almost the largest, while CER is relatively small. 90° fiber orientation produced the largest CER, and most of the other worn characters are at high level. In contrast, all of the worn characters are the least when cutting 135° ply except that CER is only next to 90° . The differences in the worn profiles are due to the different contact states and cutting stress distribution of the tool at variable

fiber orientations, which will be discussed in detail in the next section combing with the cutting mechanism.

4.3. Wear mechanism

The wear mechanism of tool has a great correlation with the cutting mechanism of CFRP. A series of simulations in different wear stages were conducted to have an intuitive understanding of wear evolution.

4.3.1. When $\theta = 0^\circ$

When $\theta = 0^\circ$, Fig. 11 presents the simulations of fresh tool and worn tools after feeding 25, 100 and 500 mm. At the initial cutting stage, Fig. 11(a) indicates that debonding between

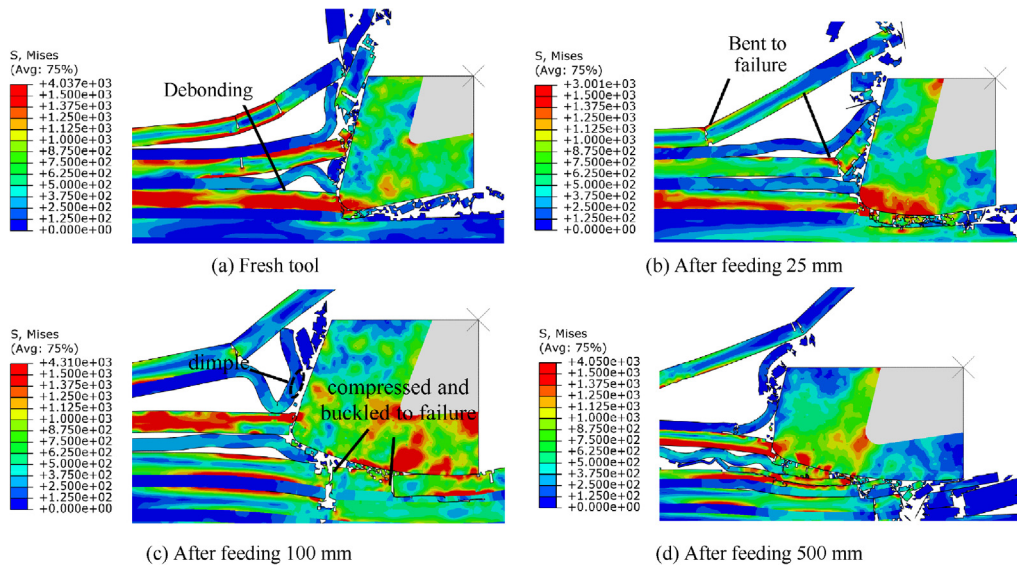


Fig. 11 Simulations of cutting process when $\theta = 0^\circ$.

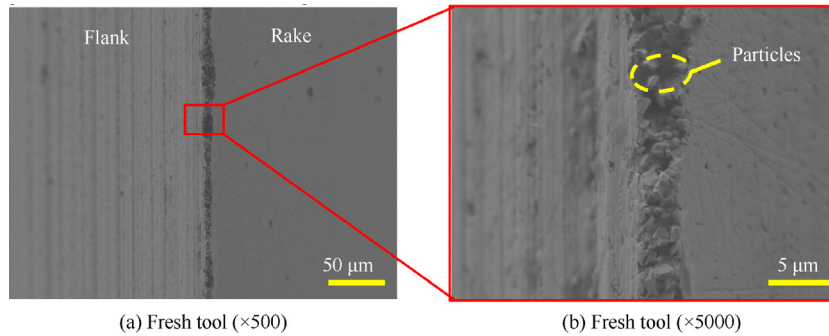


Fig. 12 SEM images of the cutting edge of fresh tool.

fibers and matrix occurs first due to the low interface strength, then the material above the cutting edge is lifted up along the rake face and bent to failure. As a result, the rake face away from cutting edge experiences little and discontinuous interaction from the chips, leading to a small amount of wear. It is noted that the debonding surface is over the tool-workpiece interface, so the fibers beneath the debonding surface have different failure mode, they are compressed and buckled to failure under the action of tool. In this process, cutting stress concentrates in the region inclining to flank face side as shown in Fig. 11(a), the fracture surfaces of fibers exert a significant abrading action to cutting tool. Consequently, tool wear concentrates in this region.

As the tool wear, it can be seen in Fig. 11(b)–(d) that the negative clearance angle is more and more evident and the actual cutting thickness is decreased. A larger amount of fibers under the flank face are pressed and rubbed to failure, the stress here can reach 3000 to 4000 MPa, and the high stress area extends along the flank face. Correspondingly, it causes further wear in this area.

Figs. 12–13 show the corresponding tool surface and machined surface. It can be seen that there are a large number of exposed carbide particles at the sharp edge of the fresh tool (see Fig. 12(b)), which are easy to fall off. After feeding 25 mm, as shown in Fig. 13(a) and (b), the exposed carbides have fell

off and the surface on cutting edge becomes smooth. At the same time, some small pits can be found out on the worn surface, this is due to the carbide particles being pulled out because of the wear of cobalt binder during contact with the fibers.³¹ Besides, it can be seen that there are small scratches on the flank face near the cutting edge, which is considered that abrasive wear occurred under the action of falling-off carbides particles. At this instant, an actual negative clearance angle forms, which further enhances the friction between flank face and the fibers beneath the debonding surface. Thus, tool wear in this stage continues to extend along the flank face.

After feeding 100 and 500 mm, as shown in Fig. 13(e) and (h), the shapes of worn edge profile change little, and there are still lots of pits but scratches on the flank face are significantly reduced. CER of the worn edge is still small, which is a reason for that the cutting force does not increase obviously. Under the action of the fibers beneath the debonding surface, the area of flank wear is enlarged a lot. Resulting in the large increase of thrust force and lots of fractured short fibers on the machined surface, as shown in Fig. 13(c), (f), (i).

Interestingly, it can be observed from Fig. 14 that small dimples range from 7 μm to 9 μm appear on the rake face near the cutting edge, which cannot be observed from any other orientations. It is due to the abrasion effect by the buckled-failure fibers ahead of the edge, as shown in Fig. 11(c).

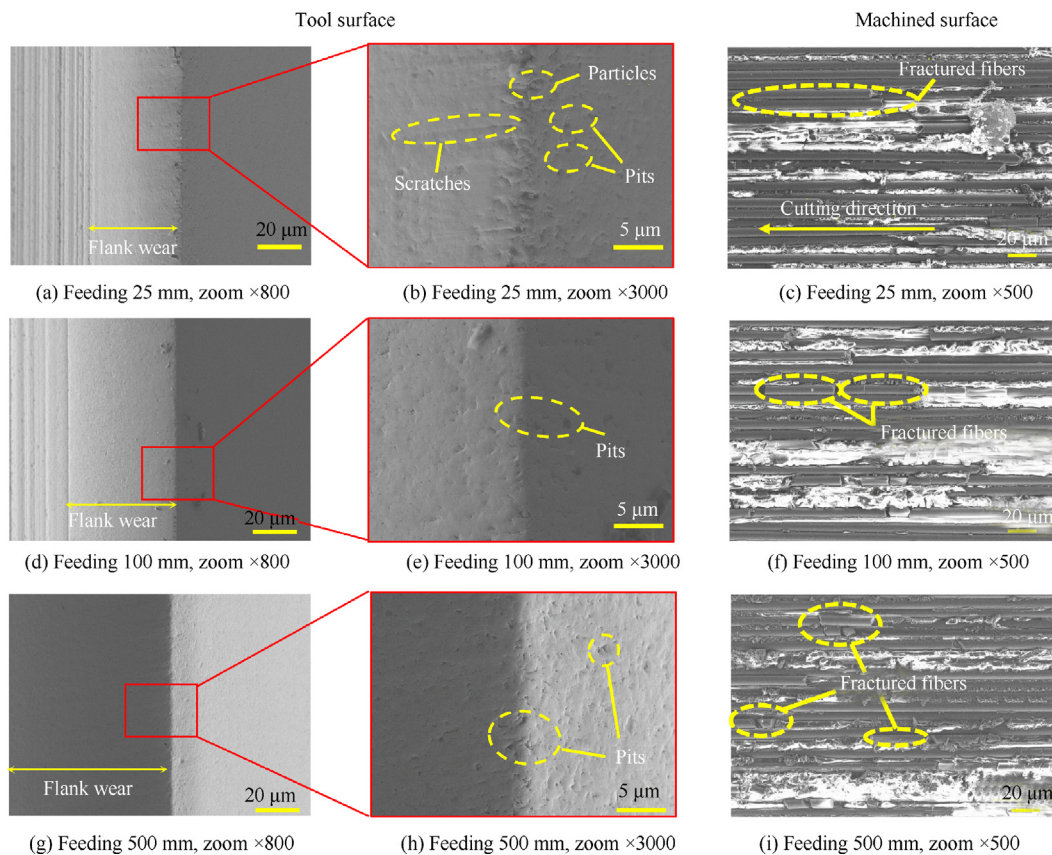


Fig. 13 SEM images of worn tools and machined surfaces after feeding 25 mm, 100 mm and 500 mm when $\theta = 0^\circ$.

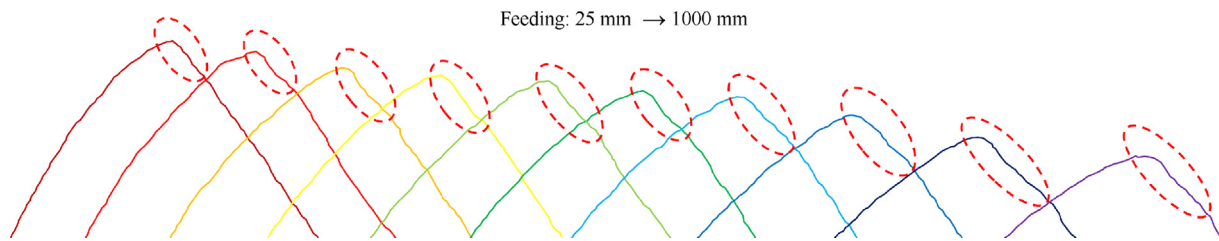


Fig. 14 Small dimples on the rake face when $\theta = 0^\circ$.

4.3.2. When $\theta = 45^\circ$

For the fresh tool at the initial cutting stage, the fibers ahead of the cutting edge are sheared to failure, then debonding occurs along the fiber orientation and cutting chip forms at last (as shown in Fig. 15(a)). Under the flank face, the broken fibers spring back to a certain extent, and the rebound direction is just opposite to the forward direction of the tool, which leads to continuous rubbing between the tool and fractured fibers as well as the concentrated stress on flank face. Besides, the combined effects of shear stress perpendicular to fiber orientation of 45° and the fiber spring-back bring about the maximum thrust force at 45° . The situations for the worn tool after feeding 25 mm are similar to those for the fresh tool, except that a larger flank wear, as shown in Fig. 15(b).

With the cutting process, the region of flank wear increases continuously, when the feeding distance reaches 500 mm, most of the fibers ahead of the cutting edge are not only sheared by

the tool, but also bended and compressed to failure (Fig. 15(d)), which leading to severe sub-surface damage.

Fig. 16 presents the SEM images of tools and machined surfaces after feeding 25, 100 and 500 mm. The evolution of worn morphologies of tool at different wear stages at 45° is similar to that at 0° . It can be seen from Fig. 16(c), (f), (i) that with the tool wear, the number of fibers fractured by bending increases a lot and even obvious gaps occur on the machined surface after feeding 500 mm. In general, similar to 0° fiber orientation, 45° orientation produces waterfall edge profile, but the wear near cutting edge is more severe. It is related to the cutting mechanism in this case. After shearing failure, the fractured surface of every fiber exerts rubbing and abrasive action on the region on flank face near cutting edge. At the same time, cutting stress concentrate in the region near the cutting edge. So, a larger PF (i.e. a larger wear near cutting edge) is obtained at 45° than that at 0° .

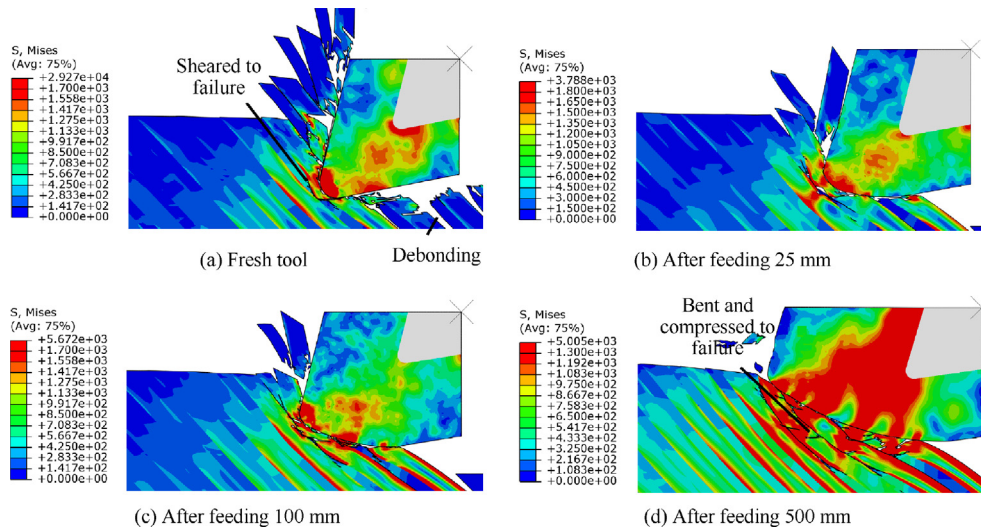


Fig. 15 Simulations of cutting process when $\theta = 45^\circ$.

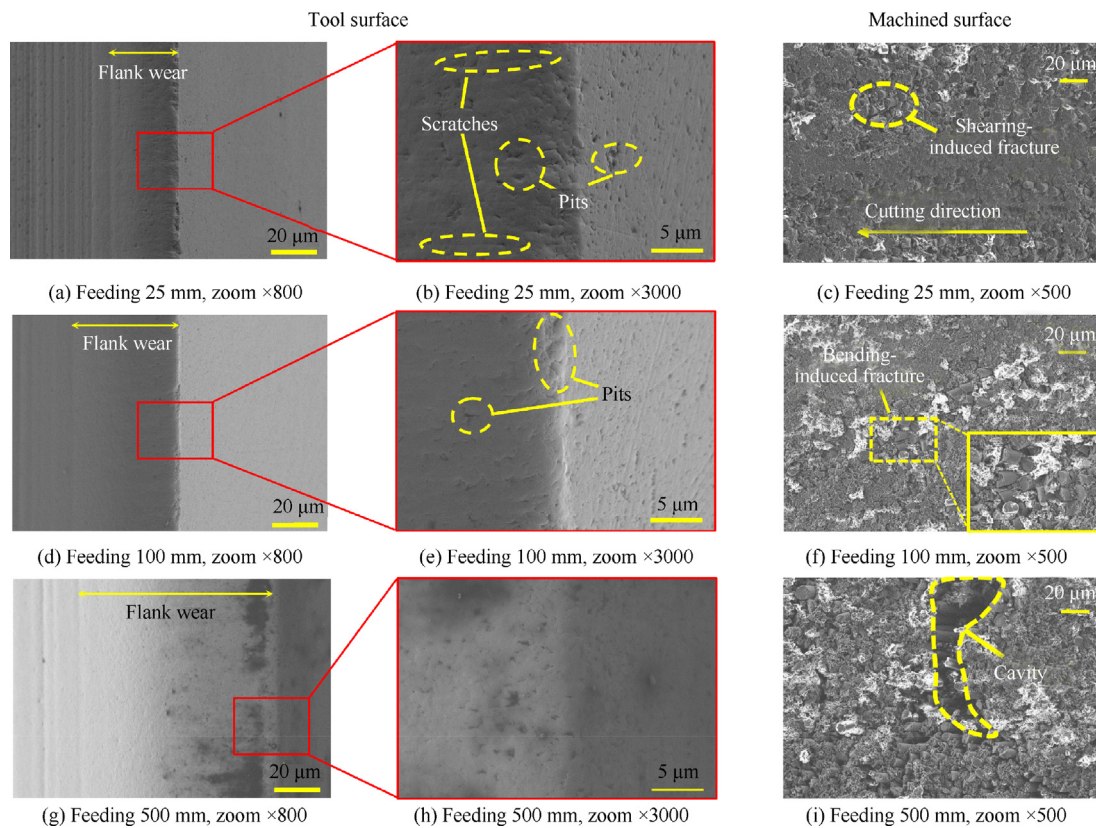


Fig. 16 SEM images of worn tools and machined surfaces after feeding 25 mm, 100 mm and 500 mm when $\theta = 45^\circ$.

4.3.3. When $\theta = 90^\circ$

According to the simulations in Fig. 17, the cutting mechanism under different wear stages can be obtained. At the initial wear stage, fibers in the cutting region are subjected to bending firstly, then the cracks appear when the strength exceeds the shear strength or bending strength, at last the chips are forced to move along the rake face. Most bending-induced cracks occurs under the cutting surface, resulting in sub-surface dam-

age and worse surface quality compared to that at 45° orientation. In the chip formation process, debonding occurs along the fiber orientation, however, due to that the fiber is perpendicular to feeding direction, the movement of chips along rake face is more difficult compared with that at 45° orientation, resulting in severe compress in the region near cutting edge inclining to rake face side. Combined with the pressing and rubbing action of the fibers under flank face, wear concentrates

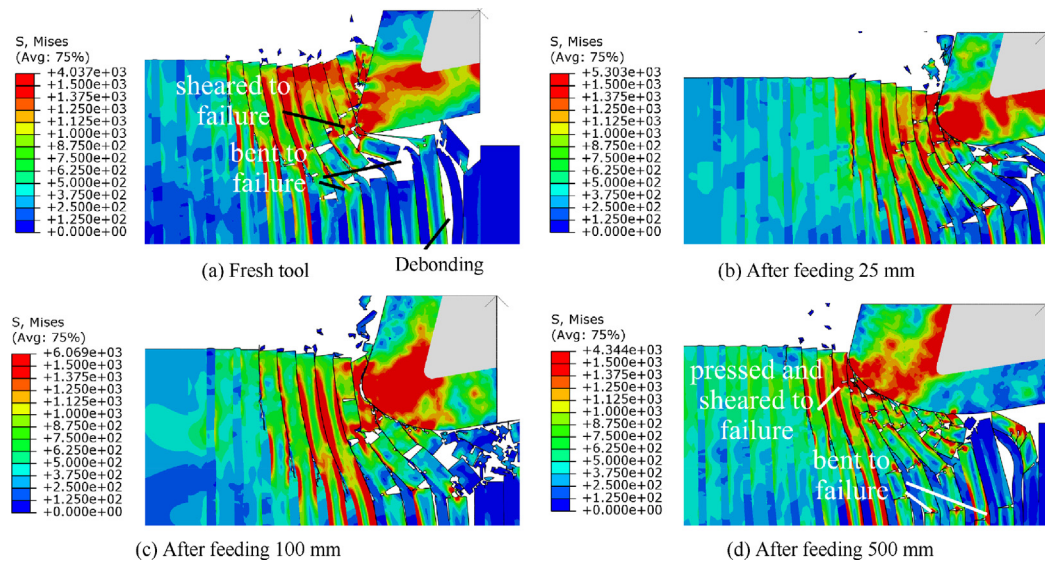


Fig. 17 Simulations of cutting process when $\theta = 90^\circ$.

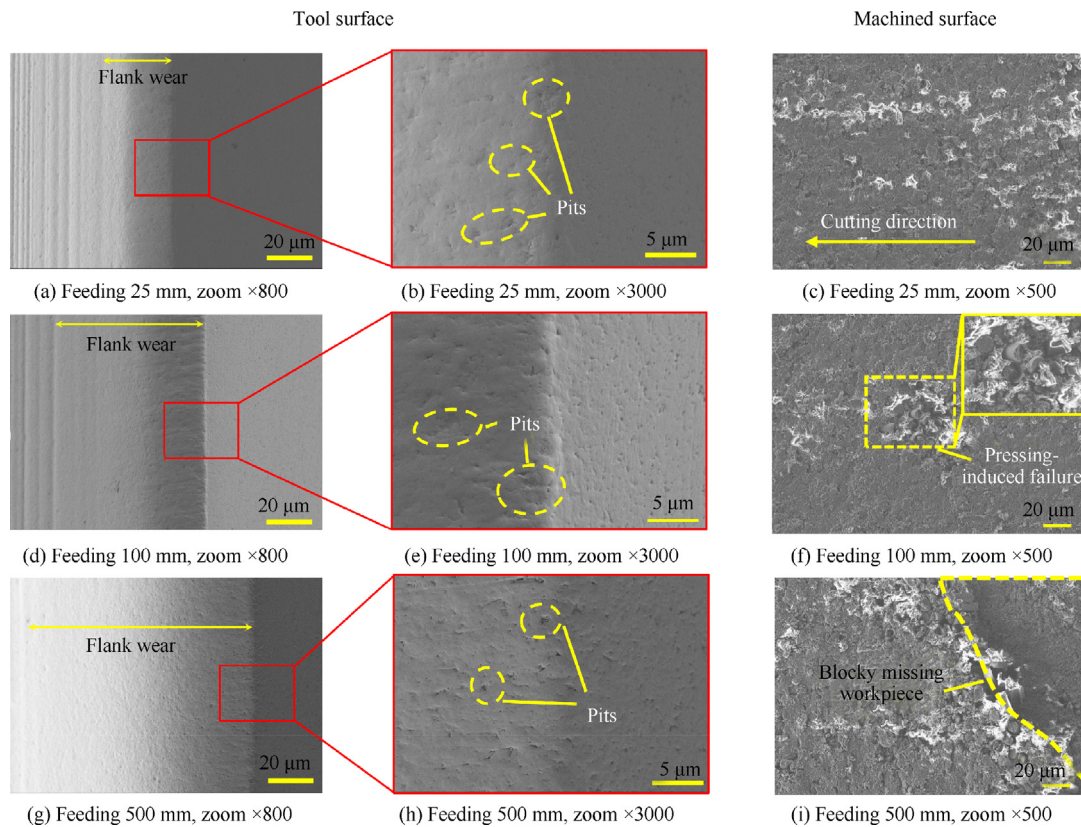


Fig. 18 SEM images of worn tools and machined surfaces after feeding 25 mm, 100 mm and 500 mm when $\theta = 90^\circ$.

around cutting edge, leading to a large CER (see Figs. 9–10). In addition, due to the sub-surface bending failure of fibers, the abrasive action on flank face is actually reduced. Therefore, the width of flank wear (VB) at 90° orientation is less than that at 0° and 45° orientations, as shown in Figs. 9–10.

With the increase of tool wear, CER continues to increase, and fibers in front of cutting edge suffer large pressing stress.

Combined with Fig. 17(b)–(d), the actual negative clearance angle of the tool increases continuously, resulting in the decrease of the actual cutting depth, both pressing-failure and shearing-failure may occur simultaneously. The sub-surface bending-failure for fibers under flank face become more severe and a large amount of chipped fibers are produced.

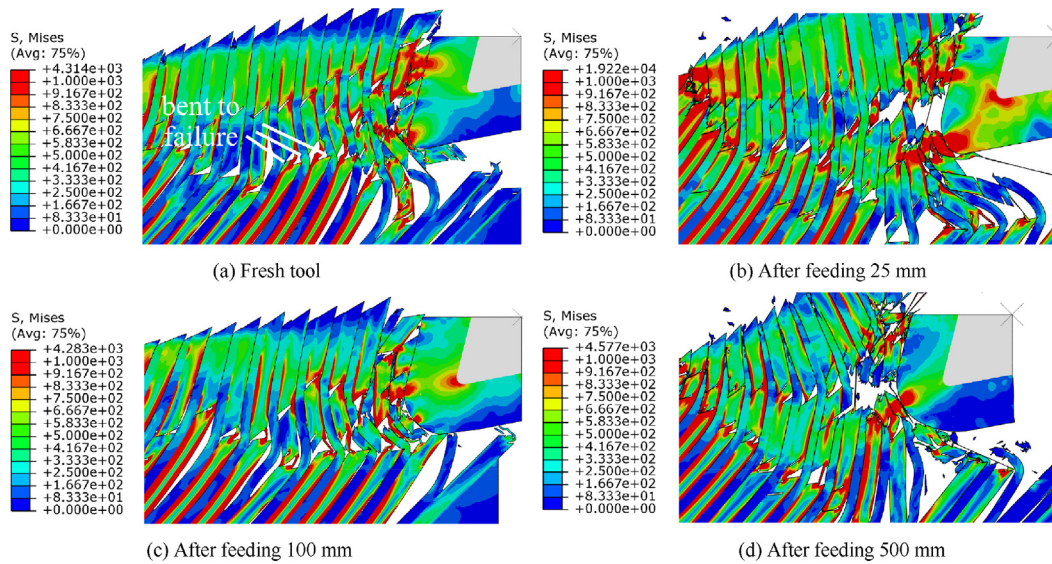


Fig. 19 Simulations of cutting process when $\theta = 135^\circ$.

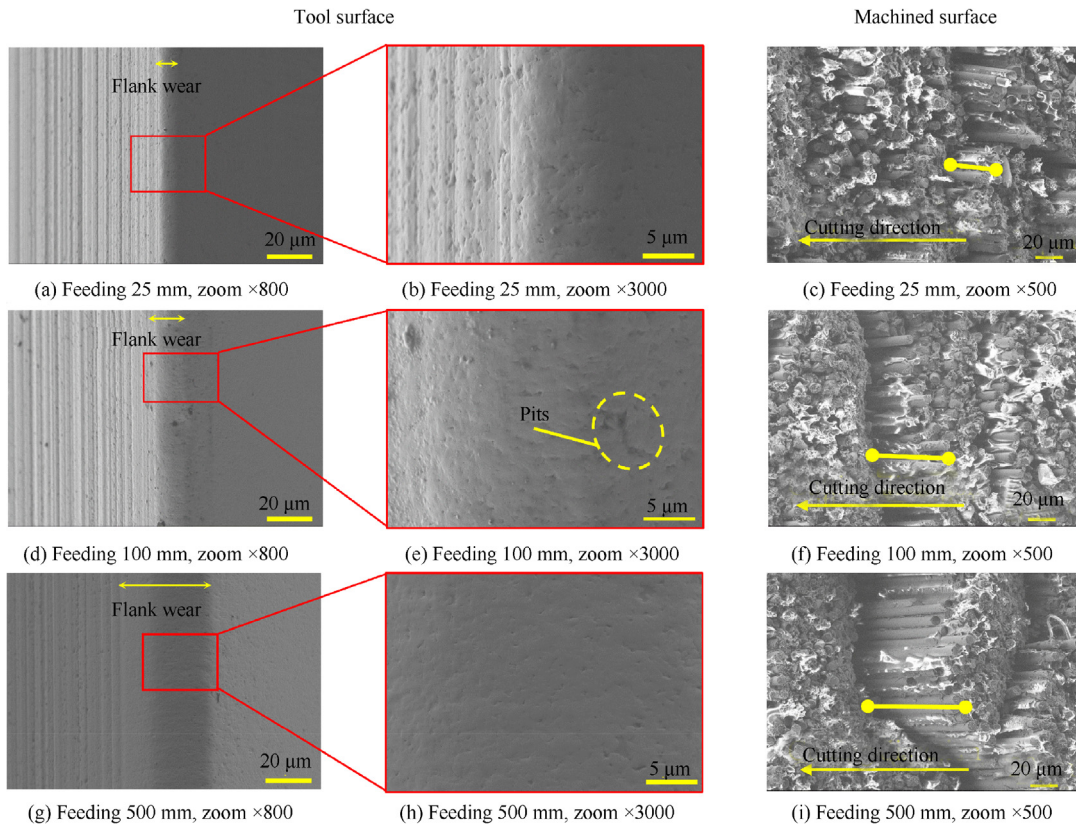


Fig. 20 SEM images of worn tools and machined surfaces after feeding 25 mm, 100 mm and 500 mm when $\theta = 135^\circ$.

The SEM images of tools and machined surfaces after feeding 25, 100 and 500 mm when $\theta = 90^\circ$ are shown in Fig. 18. There is little difference in the worn morphologies of tool at different wear stages compared to those at 0° and 45° . Under the abrasion of chipped fibers, flank wear increases gradually.

Besides, machined surface also deteriorates due to severe sub-surface bending-failure of fibers with tool wear, as shown in Fig. 17(d), more and deeper cracks occur, resulting in fiber pull-out and even a large blocky missing workpiece at the late wear stage, as shown in Fig. 18 (c), (f), (i).

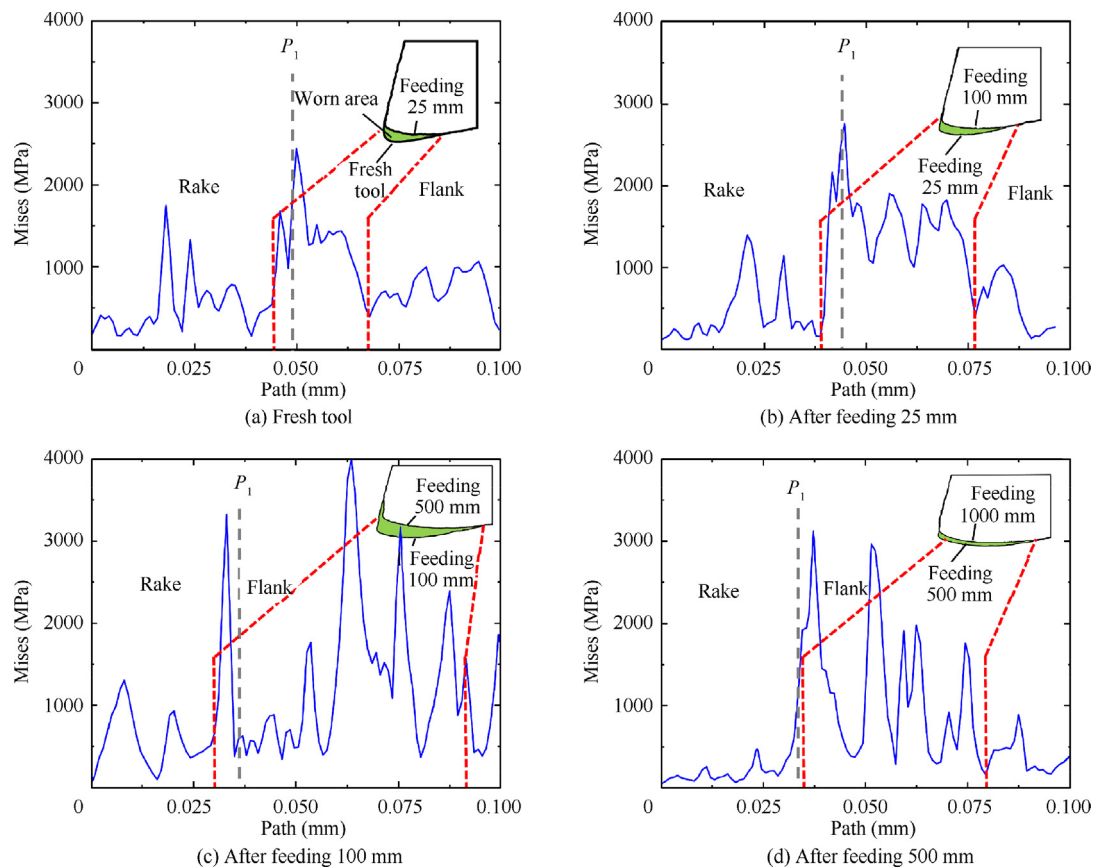


Fig. 21 Stress distribution of tool surface and corresponding profiles when $\theta = 0^\circ$.

4.3.4. When $\theta = 135^\circ$

When a new tool is used in cutting 135° ply (see Fig. 19(a)), as the tool moves forward, all of the fibers experience bending failure, but the fracture point is located below the cutting surface. In this process, the rake face has a serious compress effect on the fibers, while the flank face of the tool can hardly contact with the workpiece. Consequently, cutting stress and wear concentrate on the rake face near the cutting edge and the wear of the flank face is much smaller at the early wear stage compared with that at other fiber orientations, as shown in Fig. 9(d).

With the increase of tool wear, the cutting mechanism is almost the same. The high stress area gradually transfers to the part on the flank face near the edge, resulting in a relatively uniform tool profile, CER continues to increase. The large edge rounding at late wear stage can lead to the contact and abrasion action of the broken fibers on flank face (see Fig. 19(d)), thus flank wear increases a lot after feeding 1000 mm (see Fig. 9(d)).

The SEM images of worn tools after feeding 25, 100 and 500 mm are shown in Fig. 20(a), (d) and (g), the grinding textures on the flank face, which is produced during tool production process, can be clearly seen even after feeding 500 mm. It is another evidence that flank wear at 135° fiber orientation is small. There are no obvious horizontal scratches like Fig. 13 (b), which is attributed to the little action of fall-off WC particles at the initial cutting stage on flank face. Fig. 20(c), (f) and (i) show the machined surfaces, severe sub-surface damage occurs at the beginning of cutting process, with the tool wear,

the scale of sub-surface damage increases due to the blunt cutting edge, which can be also seen from the simulation results in Fig. 19.

Compare the tool surface stress distribution under four fiber orientations, it is not difficult to find that the cutting mechanism determines the stress distribution, which leads to different tool wear. The order of peak of surface stress is as follows: 45° , 90° , 135° , and 0° , which is just consistent with the order of the tool wear.

4.4. Discussion

Different fiber orientations lead to different tool wear profiles of cutting edge, as shown in Fig. 9, which is also observed in other studies.^{14,15} Based on the simulation results (Figs. 11, 15, 17 and 19), the different wear profiles are mainly related to the stress at different cutting stages. In order to observe the tool surface stress more obviously, the stresses along the cutting edge are extracted using the method shown in Fig. 2 and compared.

When $\theta = 0^\circ$, the surface stress distribution and the corresponding profiles of the tools are shown in Fig. 21. It can be seen that when using a new tool the stress on the flank face is generally higher than that on the rake face. This is due to the fact that the bent fibers are peeled off after a short contact with the rake face, while the flank face continues to rub against the machined surface. Combined with Fig. 11(a), the fracture surfaces of fibers exert a significant abrading action to cutting

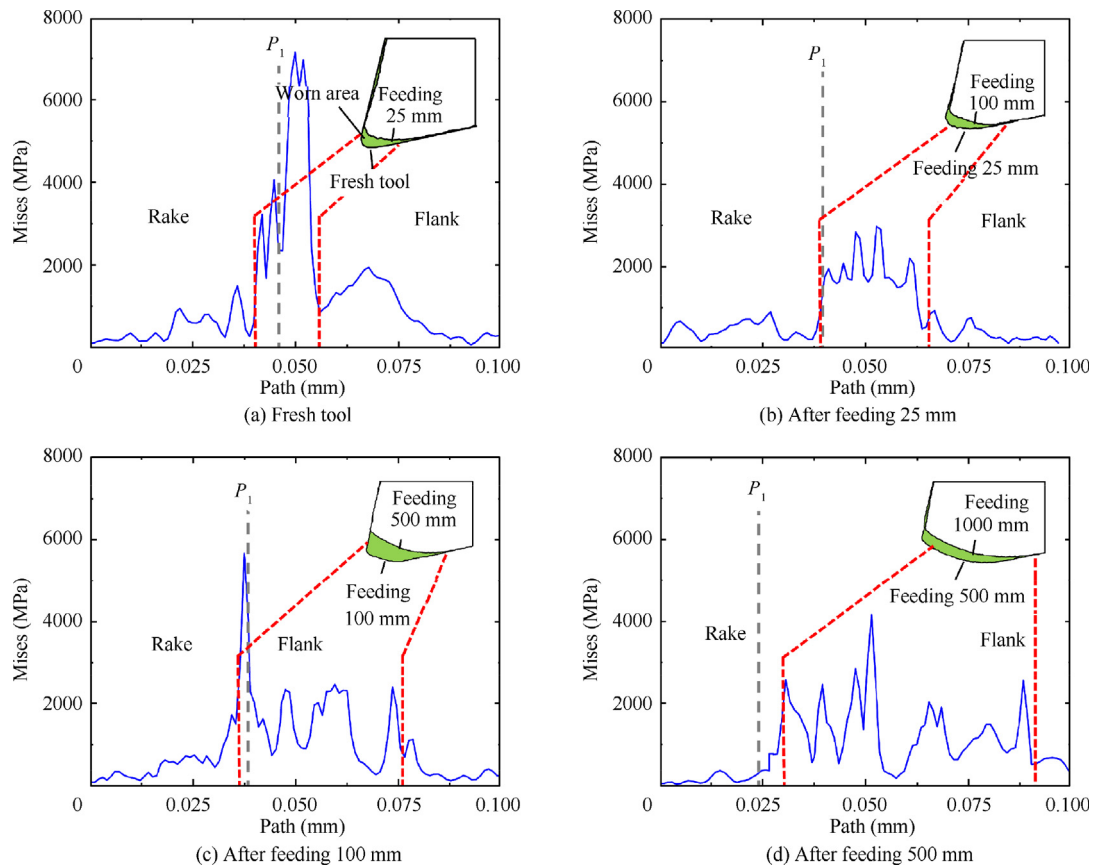


Fig. 22 Stress distribution of tool surface and corresponding profiles when $\theta = 45^\circ$.

tool, resulting in the stress concentration in the region inclining to flank face side, which is consistent with the worn profile of tool. With the process of tool wear, the flank wear increases gradually, and more fibers below the cutting plane are squeezed by the flank face (Fig. 11), which intensifies the wear of the flank face, thus, the thrust force also increases. Nguyen et al. have a similar conclusion.¹⁵ Due to the uneven wear of the rake and flank faces, the waterfall cutting edge is formed.

When $\theta = 45^\circ$, Fig. 22 shows the stress distribution of the tool surface. When using the fresh tool, it can be seen that the stress is mainly concentrated near the cutting edge, and the stress on the rake face is very small, which is due to the small contact area between the rake face and the chips. The highest stress point (higher than 6000 MPa) at the cutting edge is due to the fact that the tool meshes in simulation were set as unable to delete, which contacts with the sharp fractured fibers, resulting in a large stress concentration. Compared to $\theta = 0^\circ$, the cutting edge close to the rake face has a serious extrusion effect on the fibers during the cutting process, so the rake face wear is relatively worse. With the tool wear, the actual negative rake angle gradually increases, it significantly increases the wear on the flank face than that on the rake face, resulting in waterfall shape.

When $\theta = 90^\circ$, the stress distribution of the tool surface is depicted in Fig. 23. Different from that at 0° and 45° , at the initial wear stage the high stress is not only distributed on the flank face, but the area near the cutting edge on the rake face, the wear degree of rake face and flank face is similar,

causing the increase of CER (Fig. 10(e)). This is due to the strong squeezing effect of the rake face on the fiber during the cutting process.²⁴ With the tool wear, the sub-surface bending-failure for fibers under flank face become more severe. But the broken fibers cannot be removed timely, they are laid on the cutting surface as shown in Fig. 17, resulting in the serious scratch between the flank surface and short fibers, so the wear of the flank face is increasing, the high stress area of the flank face also increases (Fig. 23(b)–(d)). Thus, the combined shape of waterfall edge and round edge is formed, Henerichs also get the similar shape.³²

When $\theta = 135^\circ$, Fig. 24 shows the stress distribution of the tool surface. During the cutting process, the fibers are bent to failure under the action of the tool rake face.⁹ Therefore, at the beginning of cutting the stress on the rake face is larger and the wear is correspondingly severer, as shown in Fig. 24(a). The high stress area is concentrated in the cutting edge close to the rake face, and the stress on the rake face is very small. As the tool moves, the flank face begins to contact the machined surface and is scratched by broken fibers. As a result, the high stress area moves towards to flank face, but the scale is relatively small, the round edge is gradually formed.

Compare the tool surface stress distribution under four fiber orientations, it is not difficult to find that the cutting mechanism determines the stress distribution, which leads to different tool wear. The order of peak of surface stress is as follows: 45° , 90° , 135° , and 0° , which is just consistent with the order of the tool wear. The results are similar to that from

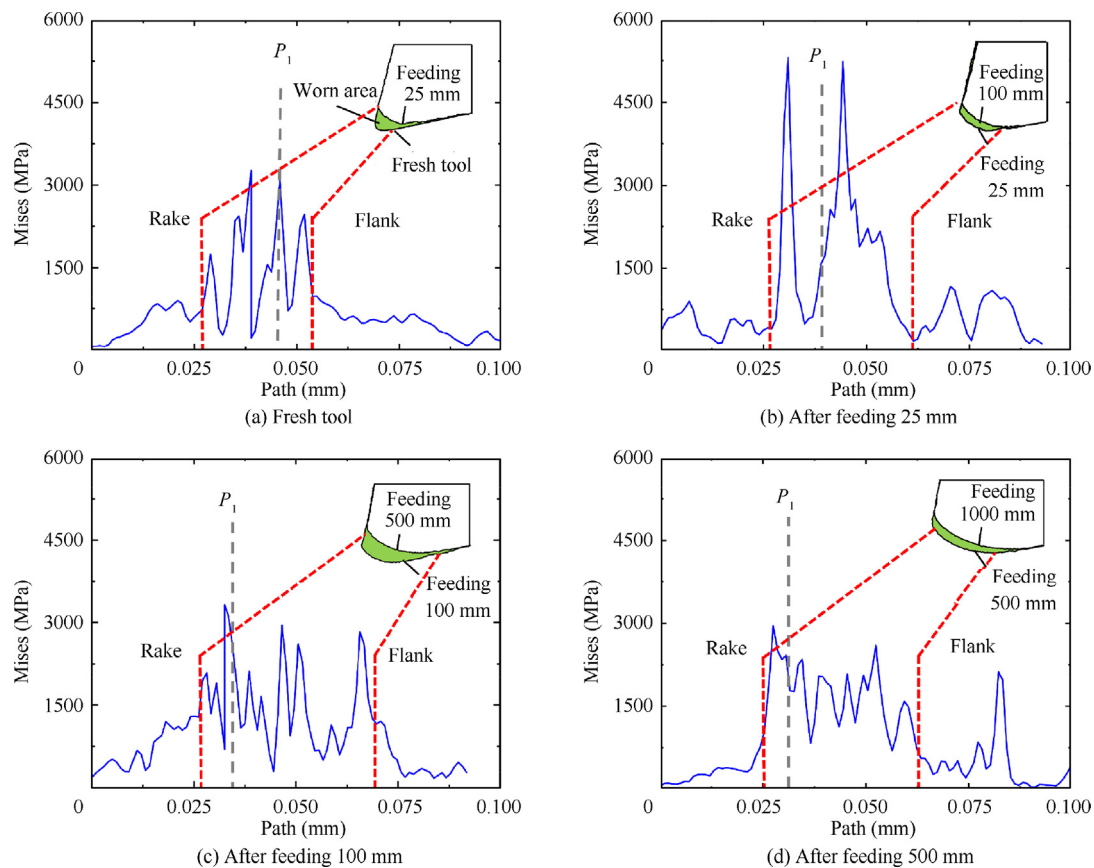


Fig. 23 Stress distribution of tool surface and corresponding profiles when $\theta = 90^\circ$.

Dold,³³ who considers that 30° fiber orientation shows largest wear. But some researches have different results,¹⁵ they believe that the least wear is obtained when $\theta = 0^\circ$, this maybe related to the set up of experiments, the use of small-diameter milling tool leads to a large variation of actual fiber cutting angle during the milling process, while a relatively small range when using large-diameter milling tool.

In the actual process of cutting CFRP, unidirectional plates are rarely used directly, usually the multidirectional plates. Because different fiber orientations have different effects on tool wear, the tool has different profiles corresponding to the position of different layers,³⁴ it is not benefit to the tool life. It may be possible to move the tool along the ply direction to make the tool wear uniformly and reduce the severe wear in some orientations, which needs to be further studied.

5. Conclusion

This paper has investigated the tool wear evolution and related mechanism when cutting of UD-CFRP. A series of simulations were conducted to obtain a lucid comprehension on the wear mechanisms. Paths are defined to analyze stress distribution qualitatively, while the 2D profiles are obtained to analyze the extent of tool wear quantitatively. Based on the experimental and numerical results, the following conclusions have been drawn.

- (1) The cutting force is related to the fracture mode of the fibers. The highest level of cutting force is produced when cutting 45° and 90° plies while the least is pro-

duced at 135° . However, the thrust force is mainly related to the rebound of fibers and the extrusion of worn tools on fibers below the cutting surface, the highest thrust force is obtained when cutting with 45° fiber orientation.

- (2) The tool wear profile varies greatly with different fiber orientations. Severe tool wear occur when cutting 45° and 90° plies, followed by 0° , while the least wear is obtained when $\theta = 135^\circ$. Besides, the tool wear stage is also a vital factor for tool wear profile, the wear position is different in different wear stages.
- (3) The stress distribution on the tool surface is determined by the cutting mechanism, and it is highly consistent with the wear area. The distribution of high stress area on the tool surface determines the position of tool wear, and the magnitude of stress determines the degree of tool wear.
- (4) The cutting mechanisms are not only related to fiber orientation but also tool wear stage. With the tool wear, more fibers are compressed or bent to failure instead of sheared to failure under the action of worn flank face. It leads to chipped fibers and severe damage in sub-surface.

Declaration of Competing Interest

The authors declare that they have no known competing financial interests or personal relationships that could have appeared to influence the work reported in this paper.

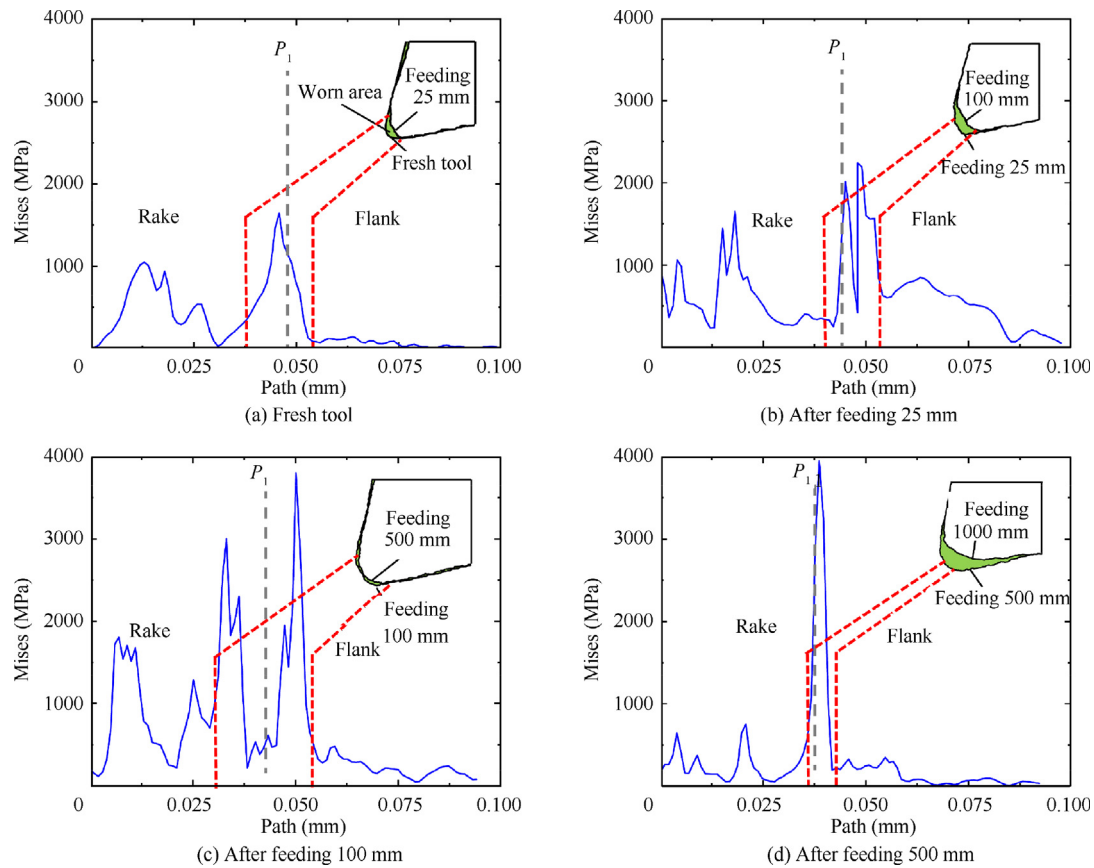


Fig. 24 Stress distribution of tool surface and corresponding profiles when $\theta = 135^\circ$.

Acknowledgements

This work was supported by the National Natural Science Foundation of China (No. 52075380) and the Natural Science Foundation of Tianjin (Nos. 21JCYBJC00610 and 19JCYBJC19000).

References

- Sun WY, Zhang DH, Luo M, et al. Machining process monitoring and application: a review. *J Adv Manuf Sci Technol* 2021;**1**(2):2021001.
- Towsyfan H, Biguri A, Boardman R, et al. Successes and challenges in non-destructive testing of aircraft composite structures. *Chin J Aeronaut* 2020;**33**(3):771–91.
- Aamir M, Tolouei-Rad M, Giasin K, et al. Recent advances in drilling of carbon fiber-reinforced polymers for aerospace applications: a review. *Int J Adv Manuf Technol* 2019;**105**(5):2289–308.
- Asmael M, Safaei B, Zeeshan Q, et al. Ultrasonic machining of carbon fiber-reinforced plastic composites: a review. *Int J Adv Manuf Technol* 2021;**113**(11):3079–120.
- Thakur A, Pal Singh A, Sharma M. Mechanics of delamination-free drilling in polymer matrix composite laminates: a review. *Proc Inst Mech Eng C J Mech Eng Sci* 2021;**235**(1):136–60.
- Buse H, Feinle P. Model system studies of wear mechanisms of hard metal tools when cutting CFRP. *Procedia Eng* 2016;**149**:24–32.
- Wang X, Kwon PY, Sturtevant C, et al. Comparative tool wear study based on drilling experiments on CFRP/Ti stack and its individual layers. *Wear* 2014;**317**(1–2):265–76.
- Wang DH, Ramulu M, Arola D. Orthogonal cutting mechanisms of graphite/epoxy composite. Part I: unidirectional laminate. *Int J Mach Tools Manuf* 1995;**35**(12):1623–38.
- An QL, Cai CY, Cai XJ, et al. Experimental investigation on the cutting mechanism and surface generation in orthogonal cutting of UD-CFRP laminates. *Compos Struct* 2019;**230**:111441.
- Meng QX, Cai J, Cheng H, et al. Investigation of CFRP cutting mechanism variation and the induced effects on cutting response and damage distribution. *Int J Adv Manuf Technol* 2020;**106**(7):2893–907.
- Rawat S, Attia H. Wear mechanisms and tool life management of WC-Co drills during dry high speed drilling of woven carbon fibre composites. *Wear* 2009;**267**(5–8):1022–30.
- Azmi AI, Lin RJT, Bhattacharyya D. Tool wear prediction models during end milling of glass fibre-reinforced polymer composites. *Int J Adv Manuf Technol* 2013;**67**(1):701–18.
- Ramirez C, Poulachon G, Rossi F, et al. Tool wear monitoring and hole surface quality during CFRP drilling. *Procedia CIRP* 2014;**13**:163–8.
- Maegawa S, Morikawa Y, Hayakawa S, et al. Effects of fiber orientation direction on tool-wear processes in down-milling of carbon fiber-reinforced plastic laminates. *Int J Autom Technol* 2015;**9**(4):356–64.
- Nguyen D, Bin Abdullah MS, Khawarizmi R, et al. The effect of fiber orientation on tool wear in edge-trimming of carbon fiber reinforced plastics (CFRP) laminates. *Wear* 2020;**450–451**:203213.
- Song DL, Li Y, Zhang KF, et al. Micromechanical analysis for microscopic damage initiation in fiber/epoxy composite during interference-fit pin installation. *Mater Des* 2016;**89**:36–49.
- Wang FJ, Wang XN, Yang R, et al. Research on the carbon fibre-reinforced plastic (CFRP) cutting mechanism using macroscopic

- and microscopic numerical simulations. *J Reinf Plast Compos* 2017;**36**(8):555–62.
18. Hassouna A, Mzali S, Zemzemi F, et al. Orthogonal cutting of UD-CFRP using multiscale analysis: finite element modeling. *J Compos Mater* 2020;**54**(18):2505–18.
 19. Abena A, Soo SL, Essa K. A finite element simulation for orthogonal cutting of UD-CFRP incorporating a novel fibre-matrix interface model. *Procedia CIRP* 2015;**31**:539–44.
 20. Su YL. Effect of the cutting speed on the cutting mechanism in machining CFRP. *Compos Struct* 2019;**220**:662–76.
 21. Hashin Z. Failure criteria for unidirectional fiber composites. *J Appl Mech* 1980;**47**(2):329–34.
 22. Yan XY, Reiner J, Bacca M, et al. A study of energy dissipating mechanisms in orthogonal cutting of UD-CFRP composites. *Compos Struct* 2019;**220**:460–72.
 23. Jiang HY, Ren YR, Liu ZH. Micro- and macro-scale simulation for axial cutting machining behaviors of 2D tri-axially braided composites. *Int J Mech Sci* 2019;**156**:1–13.
 24. Chen R, Li SJ, Li PN, et al. Effect of fiber orientation angles on the material removal behavior of CFRP during cutting process by multi-scale characterization. *Int J Adv Manuf Technol* 2020;**106**(11):5017–31.
 25. Raj DS, Karunamoorthy L. A new and comprehensive characterisation of tool wear in CFRP drilling using micro-geometry and topography studies on the cutting edge. *J Manuf Process* 2018;**32**:839–56.
 26. Abena A, Soo SL, Essa K. Modelling the orthogonal cutting of UD-CFRP composites: development of a novel cohesive zone model. *Compos Struct* 2017;**168**:65–83.
 27. Voss R, Seeholzer L, Kuster F, et al. Analytical force model for orthogonal machining of unidirectional carbon fibre reinforced polymers (CFRP) as a function of the fibre orientation. *J Mater Process Technol* 2019;**263**:440–69.
 28. Abena A, Essa K. 3D micro-mechanical modelling of orthogonal cutting of UD-CFRP using smoothed particle hydrodynamics and finite element methods. *Compos Struct* 2019;**218**:174–92.
 29. Li CP, Zhao YF, Qiu XY, et al. Interface mechanical damage mechanism in machining carbon fiber-reinforced plastic/Ti stacks based on a three-dimensional microscopic oblique cutting model. *Compos Struct* 2022;**279**:114737.
 30. Calzada KA, Kapoor SG, DeVor RE, et al. Modeling and interpretation of fiber orientation-based failure mechanisms in machining of carbon fiber-reinforced polymer composites. *J Manuf Process* 2012;**14**(2):141–9.
 31. Muhamad Khairussaleh NK, Che Haron CH, Ghani JA. Study on wear mechanism of solid carbide cutting tool in milling CFRP. *J Mater Res* 2016;**31**(13):1893–9.
 32. Henerichs M, Voß R, Kuster F, et al. Machining of carbon fiber reinforced plastics: influence of tool geometry and fiber orientation on the machining forces. *CIRP J Manuf Sci Technol* 2015;**9**:136–45.
 33. Dold C, Henerichs M, Bochmann L, et al. Comparison of ground and laser machined polycrystalline diamond (PCD) tools in cutting carbon fiber reinforced plastics (CFRP) for aircraft structures. *Procedia CIRP* 2012;**1**:178–83.
 34. Kim M, Lee M, Cho G, et al. Effect of the fiber orientation and the radial depth of cut on the flank wear in end milling of CFRP. *Int J Precis Eng Manuf* 2020;**21**(7):1187–99.

2022-09-07

Effects of fiber orientation on tool wear evolution and wear mechanism when cutting carbon fiber reinforced plastics

Wu, Weizhou

Elsevier

Wu W, Li S, Qin X, et al., (2022) Effects of fiber orientation on tool wear evolution and wear mechanism when cutting carbon fiber reinforced plastics. Chinese Journal of Aeronautics, Available online 7 September 2022

<https://doi.org/10.1016/j.cja.2022.09.003>

Downloaded from Cranfield Library Services E-Repository